



**HAL**  
open science

# Measurement of density fluctuations using digital holographic interferometry in a standing wave thermoacoustic oscillator

Guillaume Penelet, Mathieu Leclercq, Thibault Wassereau, Pascal Picart

## ► To cite this version:

Guillaume Penelet, Mathieu Leclercq, Thibault Wassereau, Pascal Picart. Measurement of density fluctuations using digital holographic interferometry in a standing wave thermoacoustic oscillator. *Experimental Thermal and Fluid Science*, 2016, 70, pp.176-184. 10.1016/j.expthermflusci.2015.09.012 . hal-02057609

**HAL Id: hal-02057609**

**<https://univ-lemans.hal.science/hal-02057609>**

Submitted on 5 Mar 2019

**HAL** is a multi-disciplinary open access archive for the deposit and dissemination of scientific research documents, whether they are published or not. The documents may come from teaching and research institutions in France or abroad, or from public or private research centers.

L'archive ouverte pluridisciplinaire **HAL**, est destinée au dépôt et à la diffusion de documents scientifiques de niveau recherche, publiés ou non, émanant des établissements d'enseignement et de recherche français ou étrangers, des laboratoires publics ou privés.

# Measurement of density fluctuations using digital holographic interferometry in a standing wave thermoacoustic oscillator.

Guillaume PENELET<sup>a</sup>, Mathieu LECLERCQ<sup>a</sup>, Thibault WASSEREAU<sup>a</sup>,  
Pascal PICART<sup>a</sup>

<sup>a</sup>*Laboratoire d'Acoustique de l'Université du Maine, UMR CNRS 6613, Avenue Olivier Messiaen, 72085 Le Mans Cedex 9, FRANCE*

---

## Abstract

This paper describes an optical set-up for measuring density fluctuations associated to acoustic oscillations in a thermoacoustic prime-mover. A time-resolved, full-field holographic interferometry technique is used, which enables to measure the optical phase difference between a reference beam and a probe beam passing through the acoustic resonator. The paper first presents the experimental set-up and the processing of holograms from which the instantaneous variations of the gas density along the line of sight of the probe beam are obtained. Then, the measurement technique is applied to the analysis of density fluctuations in the neighborhood of the heated side of a stack in a standing wave thermoacoustic prime mover during the transient regime of wave amplitude growth. The experimental results reveal that there exists very significant entrance effects, which lead to the generation of higher harmonics as well as mean (time-averaged) mass rarefaction in the vicinity of the stack termination. Finally, a short discussion is provided, based on a simplified modeling of higher harmonics generation in temperature associated to the oscillations of an inviscid gas through the stack, but the model fails in explaining the magnitude of the phenomena observed.

*Keywords:* Thermoacoustics, Digital Holography

---

*Email address:* `guillaume.penelet@univ-lemans.fr` (Guillaume PENELET)

## 1. Introduction

A first approach of acoustical phenomena in fluids usually involves considering the wave process in terms of pressure and velocity fluctuations around an equilibrium state, and there exists different means to measure those quantities, such as microphones, Laser Doppler Velocimetry or Particle Image Velocimetry. However, density (as well as temperature) fluctuations always accompany pressure fluctuations, and it is sometimes worth considering to measure those density fluctuations, notably when analyzing unsteady heat and mass transfer phenomena involved in thermoacoustic engines.

The operation of thermoacoustic engines is governed by the thermoviscous interaction between gas oscillations and the solid frame of a porous material, referred to as a stack [1, 2]. This stack is usually connected to heat exchangers, and inserted within an acoustical resonator. When the thermoacoustic engine is operated as a prime-mover, the application of a temperature gradient along the stack axis leads to the generation of self-sustained acoustic oscillations at the frequency of the most unstable mode ; when the thermoacoustic engine is operated as a heat pump, the sustain of resonant gas oscillations by an adequate source leads to advective heat transport by sound along the stack axis. The design and the development of thermoacoustic engines already has a three-decade history[3] and there exists several examples of devices able to reach high performances [4, 5, 6, 7, 8, 9]. However, despite their simplicity in terms of geometry, thermoacoustic engines are not very well understood due to the complexity and the variety of the phenomena saturating the acoustic wave amplitude. Among these nonlinear phenomena are the ones impacting unsteady heat and mass transfer through the thermoacoustic core, such as acoustic streaming [10], or hydrodynamic/thermal entrance effects occurring notably at the stack termination (vortex shedding[11], transitional turbulence[12], nonlinear temperature fluctuations[13]).

Because of the complexity of the phenomena involved in thermoacoustics, it is useful to develop adequate measurement techniques allowing to get more information than the one a microphone could provide. Laser Doppler Velocimetry and Particle Image Velocimetry provide information about the gas parcel velocity and have been used previously to characterize acoustic streaming [14, 15, 16, 17] or vortex shedding processes [18, 19, 20], while cold wire anemometry[21] has been used to characterize the nonlinear temperature fluctuations in the vicinity of the stack termination. In this paper, attention is focused on the development of another measurement method

38 allowing to get information about density fluctuations from the variations  
39 of the optical index of the gas. This technique basically consists of an in-  
40 terferometer in which optical phase variations are obtained from a full-field,  
41 time-resolved digital holography technique.

42 Thanks to the development of high resolution CCD cameras and the  
43 increasing power of computers, digital holographic/interferometric measure-  
44 ments are nowadays under development and have already been used to ana-  
45 lyze various processes of vibration kinematics [22, 23] or fluid mechanics[24],  
46 but only a few works have been made to characterize the density fluctuations  
47 associated to an acoustic process. There exists pioneering works performed  
48 fifteen years ago by Wetzal and Herman[25, 26, 27], in which analog hologra-  
49 phy has been used to measure temperature fluctuations at the end of a couple  
50 of parallel plates submitted to a high amplitude acoustic field. Interferomet-  
51 ric techniques have also been used recently to characterize different classes of  
52 thermoacoustic phenomena, like sound generation by unsteady heat release  
53 within a flame[28], or the so-called piston effect generated in a small cell  
54 filled with critical CO<sub>2</sub> [29], but these techniques only allowed the analysis of  
55 local (i.e. non full-field) density fluctuations. It is therefore worth consider-  
56 ing to pursue the development of these techniques to get further information  
57 about various thermoacoustic phenomena, and more generally about some  
58 physical processes in which the derivation of density from pressure is not  
59 straightforward.

60 The device under consideration in this paper [see Fig. 1(a)] is a quarter-  
61 wavelength thermoacoustic prime-mover, which simply consists of a straight  
62 duct, closed at one end, and equipped with a stack submitted to a temper-  
63 ature gradient. In the following, the measurement of density fluctuations by  
64 digital holography are performed in the vicinity of the hot side of the stack,  
65 during the transient regime of wave amplitude growth. The experimental set-  
66 up and the data processing are presented in section 2. Experimental results  
67 are presented in section 3, which enable to confirm that complicated heat  
68 and mass transfer processes are involved near the stack end. A discussion is  
69 provided in section 4, based on the comparison between experimental results  
70 and a simplified model developed by Gusev et al. [13].

## 71 2. Experimental apparatus and data processing

### 72 2.1. Experimental apparatus

73 A sketch of the thermoacoustic device under consideration in this study  
74 is presented in Fig. 1(a). It is composed of a glass tube (49 cm in length,  
75 inner diameter  $D_i = 52$  mm, outer diameter  $D_o = 60$  mm) open at one end  
76 and closed by a rigid plug at the other end. Inside the tube is inserted the  
77 cylindrical stack (48 mm in length), whose diameter fits the inner diameter  
78 of the tube. This stack is made up of a 600 CPSI (cells per square inch)  
79 ceramic catalyst with numerous square channels of section  $0.9 \times 0.9$  mm. The  
80 side of the stack facing the plug is heated using an electrical resistance wire  
81 (Nichrome wire, 36 cm in length, 0.25mm in diameter, resistivity  $7 \Omega/ft$ )  
82 regularly coiled through the stack end, and connected to a DC electrical  
83 power supply. Sound is captured using a 1/4-in. condenser microphone  
84 (model GRAS, type 40BP) flush-mounted through the plugged end of the  
85 resonator. Note that a photograph of this device can also be found in ref.  
86 [30] ; it is worth mentioning that the presence of heater does not affect the  
87 optical measurements presented in the following, because the Nichrome wire  
88 is mounted flush *inside* the stack so that the laser beam used for digital  
89 holography does not pass through the heater.

90 In this study, the position of the stack along the resonator's axis is fixed  
91 at a distance  $d = 24$  cm from the rigid plug. For this configuration, the onset  
92 of self-sustained thermoacoustic oscillations occurs as soon as the heat power  
93 supplied by the Nichrome wire exceeds the critical value  $Q_{onset} \approx 20$  W (note  
94 that this value of  $Q_{onset}$  depends on the stack position [31]). The frequency  
95  $f \approx 171$  Hz of acoustic oscillations corresponds to the quarter wavelength  
96 resonance, which means that  $f \approx c_0/4L$ , where  $c_0 \approx 344m/s$  stands for  
97 the adiabatic sound speed at room temperature. Previous studies of the  
98 same device[30, 31, 32] have clearly shown that, despite of its very simple  
99 geometry, this thermoacoustic oscillator can exhibit complicated dynamics  
100 of wave amplitude growth/saturation which are not reliably reproduced by  
101 theoretical/numerical modeling. It is therefore the objective of this study to  
102 perform holographic interferometry to analyze the refractive index variations  
103 in a window localized near the stack, where the temperature gradients are  
104 the highest, and to gain further insight on the physical processes controlling  
105 the saturation of the thermoacoustic instability.

106 A sketch of the optical set-up used to perform the measurement of density  
107 fluctuations close to the heated side of the stack is presented in Fig. 1(b).

108 This set-up basically consists of a Fresnel interferometer enabling to measure  
109 the optical phase difference between a reference beam and a measurement  
110 beam passing through the acoustic resonator. This phase difference is caused  
111 by the variations of the refractive index within the resonator, due to both  
112 heat transport (notably the slow variations of the temperature field caused  
113 by heating) and acoustic (onset of self-sustained oscillations) processes. The  
114 light source is a laser source (Cobolt Flamenco, optical wavelength  $\lambda=660$   
115 nm). The laser beam is split into a reference beam and a probe beam, and  
116 both beams are then expanded and bundled to parallel rays by a collimating  
117 lens. The probe beam passes through the acoustic resonator next to heated  
118 side of the stack, as indicated in Fig. 1(a). Then, the interference between  
119 the reference and the probe beam are captured by two CCD sensor (thanks  
120 to a 50/50 cube), namely a CCD camera and a high speed CMOS sensor [see  
121 Fig. 1(b)]. The CCD camera (model Hamamatsu ORCA-3CCD C7780-10)  
122 is used for analyzing slow temperature variations preceding the onset of self-  
123 sustained oscillations: the CCD sensor samples the interferogram at a rate of  
124 1 im./s with  $1344 \times 1024$  pixels sized  $6.45 \mu m$ . The high speed CMOS sensor  
125 (Phantom V5.1) is used for analyzing the rapid fluctuations of the density  
126 occurring after the onset of self-sustained oscillations. This sensor is triggered  
127 when the peak amplitude of acoustic pressure exceeds the threshold value of  
128 100 Pa, thanks to the signal provided by the microphone. Interferograms are  
129 then sampled during 4 seconds at 1000 im./s with  $1024 \times 1024$  pixels sized  
130  $14.8 \mu m$ . Note that the above mentioned choice is intrinsically related to  
131 the performance of the high speed camera, which sets the bounds of both  
132 time and space resolution, so that a compromise has to be found to get the  
133 best sampling rate with a maximum number of pixels. Here, the sampling  
134 frequency of 1 kHz has been chosen so as to satisfy the Shannon-Nyquist  
135 criterium up to the second harmonic of thermoacoustic oscillations.

## 136 *2.2. Data processing*

137 The quantity of interest given by the optical set-up is the optical phase  
138 between the probe beam and the reference beam, which is related to the  
139 refractive index variation near the stack. From the optical set-up and ad-  
140 justment of the beam splitter cube, digital holograms including spatial carrier  
141 frequencies (off-axis holography) are recorded and processed. The introduc-  
142 tion of the spatial carrier frequency by the cube leads to the recording of one  
143 hologram at each instant, since there is no need for phase shifting [33]. This  
144 provided a single-shot and real-time capability to the experimental set-up to

145 investigate acoustic phenomena. Fig. 2 shows the digitally recorded holo-  
 146 gram with the left part of the image being close to the heat border of the  
 147 stack. For any optical wavelength, the recorded image plane hologram can  
 148 be expressed as [34, 35]:

$$H(x, y) = O_0(x, y) + R(x, y)O^*(x, y) + R^*(x, y)O(x, y) \quad (1)$$

149 where  $O(x, y)$  and  $R(x, y)$  are the object and the reference wave respectively.

150 For convenience  $R(x, y)$  can be represented with unitary amplitude. Ac-  
 151 counting for the spatial carrier modulation introduced by the set-up, the  
 152 hologram at optical wavelength  $\lambda$  can be written as

$$H(x, y) = O_0(x, y) + O(x, y)e^{2i\pi(u_r x + v_r y)} + O^*(x, y)e^{-2i\pi(u_r x + v_r y)}, \quad (2)$$

153 where  $2i\pi(u_r x + v_r y)$  is the spatial carrier phase modulation along the  $x - y$   
 154 coordinates of the set of reference axis [see Fig. 1(b,c)],  $O_0 = |O(x, y)|^2 +$   
 155  $|R(x, y)|^2$  is the zero order diffraction and we consider  $O = a_\lambda e^{i\varphi_\lambda}$ . The  
 156 Fourier transform of Eq. (2) leads to [36]:

$$\tilde{H}(u, v) = \tilde{O}_0(u, v) + \tilde{C}(u - u_r, v - v_r) + \tilde{C}^*(-u - u_r, -v - v_r) \quad (3)$$

157 where  $\tilde{C}$  and  $\tilde{O}_0$  are respectively the Fourier transform of  $O$  and  $O_0$ , and  
 158 where  $(u, v)$  stand for the spatial frequencies.

159 Figure 3 shows the spatial frequency of the digital hologram. The zero  
 160 order diffraction corresponds to central spot of the spectrum and the two  
 161 complex conjugated orders of (3) are localized symmetrically. The order of  
 162 interest is filtered using a binary filter centered at spatial frequencies  $(u_r, v_r)$   
 163 indicated by the red cross. The dashed line indicates the frequency limits of  
 164 the filter. If the spatial frequencies  $u_r$  and  $v_r$  are correctly adjusted, the three  
 165 orders are well separated in the spatial frequency spectrum. By applying  
 166 a bandwidth limited filter ( $\Delta u \times \Delta v$  wide) around the spatial frequency  
 167  $(u_r, v_r)$ , and after filtering and inverse 2D Fourier transform, one gets the  
 168 object complex amplitude[37]:

$$C(x, y) \cong [a_\lambda(x, y)e^{i\varphi_\lambda(x, y)}e^{2i\pi(u_r x + v_r y)}] * h(x, y) \quad (4)$$

169 where  $*$  means convolution product and where

$$h(x, y) = \Delta u \Delta v e^{2i\pi(u_\lambda + v_\lambda)} \text{sinc}(\pi \Delta u x) \text{sinc}(\pi \Delta v y) \quad (5)$$

170 is the impulse response corresponding to the filtering applied in the Fourier  
171 domain. The spatial resolution is related to  $1/\Delta u$  and  $1/\Delta v$  respectively in  
172 the x-y axis. In addition the phase recovered with Eq. (4) includes the spatial  
173 carrier modulation that has to be removed. This is achieved by multiplying  
174  $C$  by  $e^{-2i\pi(u_r x + v_r y)}$ . Note that if the image of the test section is not in focus,  
175 the refocusing can be performed using the angular spectrum transfer function  
176 to get an in-focus image [37, 38]. After the reconstruction process, both the  
177 optical phase and the amplitude can be estimated from Eq. (4):

$$\varphi_\lambda(x, y) = \arctan\left(\frac{\Im[C(x, y)]}{\Re[C(x, y)]}\right), \quad (6)$$

$$a_\lambda(x, y) = \sqrt{(\Re[C(x, y)])^2 + (\Im[C(x, y)])^2} \quad (7)$$

178 where  $\Re$  and  $\Im$  respectively stand for the real and the imaginary parts of a  
179 complex number. In Fig. 4, a sample phase map is extracted and shown : the  
180 phase is calculated modulo  $2\pi$  and exhibits phase jumps. The curvature of  
181 the isophase lines observed in Fig. 4 can be attributed, at least partially, to  
182 the refraction of optical beam through the cylindrical glass tube. The effect  
183 of the glass tube can however be suppressed by subtracting the phase map  
184 of Fig. 4 with the one obtained at a reference state, e.g. before switching on  
185 the heat supply.

186 When the test section is modified, for example due to heating and/or  
187 acoustic oscillations, a refractive index variation is induced along the object  
188 beam within the duct, and this modifies the optical path and then the optical  
189 phase. The phase change  $\Delta\varphi_\lambda = \varphi_\lambda - \varphi_\lambda^{ref}$  between a current state  $\varphi_\lambda$  and the  
190 reference state  $\varphi_\lambda^{ref}$ , namely the one without heating and acoustic oscillations,  
191 is related to the associated difference of optical index as follows

$$\Delta\varphi = \frac{2\pi L(z)}{\lambda} (\langle n \rangle - \langle n_{ref} \rangle) \quad (8)$$

192 where the notation  $\langle \dots \rangle$  refers to an average along the beam path through  
193 the waveguide [length  $L(y)$ , see Fig. 1(c)]. The mean refractive index  $\langle n \rangle$   
194 itself is related to the mean density along the line of sight, according to the  
195 Gladstone-Dale relation:

$$\langle \rho \rangle = \frac{2}{3\hat{r}} (\langle n \rangle - 1), \quad (9)$$



196 where  $\hat{r} = 0.1506 \times 10^{-3} m^3 kg^{-1}$  is the specific refractivity of air at  $\lambda =$   
197  $607nm$  (this parameter is almost independent of the optical wavelength, here  
198  $\lambda = 660nm$ ). As a result, the fluid density  $\langle \rho \rangle(x, y, t)$  can be calculated from the  
199 phase difference  $\Delta\varphi_\lambda$  using Eqs. (8) and (9). Calculating the phase difference  
200 between each recorded instant leads to a modulo  $2\pi$  phase map related both to  
201 temperature and density variations. Figure 5 shows such a phase map which  
202 cannot be used before phase unwrapping. Phase unwrapping consists in  
203 removing the  $2\pi$  phase jumps, so as to recover a continuous phase variation  
204 around the field of view [39]. Figure 6 shows the unwrapped phase map  
205 obtained after processing of phase from fig. 5, which itself allows to draw a  
206 map of the average density  $\langle \rho \rangle$ .

### 207 3. Experimental results

208 The experimental results presented hereafter are obtained for a heat  
209 power supply fixed to  $Q = 25.1$  W ( $Q > Q_{onset}$ ). The first interferogram  
210 obtained at time  $t=0$  s is defined as the reference state from which the phase  
211 difference  $\Delta\varphi_\lambda(x, y)$  is calculated. The DC power supply is then switched  
212 on, which leads around time  $t=75$  s to the onset of self-sustained acoustic  
213 oscillations at frequency  $f \approx 171$  Hz. Both the regime of heating before on-  
214 set and that of wave amplitude growth are analyzed using digital holography  
215 (using the CCD camera and the high speed CMOS sensor, respectively).

216 First of all, we analyze the evolution of density during the heating stage.  
217 Before the onset of the thermoacoustic instability, the pressure is constant  
218 and equals the atmospheric pressure at room temperature,  $P_0 = 1.015 \times$   
219  $10^5$  Pa. Due to this, it is straightforward to obtain the temperature field  
220  $\langle T_0 \rangle(x, y)$  averaged along  $z$  through the probe beam [see Fig 1(c)], using the  
221 ideal gas law

$$P_0 = \langle \rho \rangle R \langle T \rangle, \quad (10)$$

222 where  $R = 287.058$   $J.kg^{-1}.K^{-1}$  stands for the specific gas constant of air.  
223 In Fig.7, the measured increase of  $\langle T \rangle$  as a function of time is presented  
224 for different positions  $x$  along the resonator's axis. More precisely, the data  
225 presented are calculated from the interferograms obtained with the CCD  
226 sensor, and correspond to the evolution with time of the temperature  $\langle T \rangle$ ,  
227 which itself is averaged (for each sample interferogram) through a small zone  
228 of cross-sectional area  $10 \times 50$  pixels along  $x$  and  $y$ , respectively, the latter  
229 zone being itself centered at some position  $x$  along the resonator's axis. The

230 data presented are obtained for 5 different positions, from  $x = 0.3$  mm up  
 231 to  $x = 6$  mm [the reference position  $x = 0$  corresponds to the heated side of  
 232 the stack, see Fig. 1(a)]. From the results presented in Fig.7, one can clearly  
 233 see the gradual increase of the temperature, as well as the establishment  
 234 of a steep, negative temperature gradient. It is worth reminding that the  
 235 magnitudes of the temperature presented in Fig.7 are z-averaged magnitudes  
 236 along the line of sight [see Fig. 1(c)], and that these temperatures are lower  
 237 than the one we can measure using a thermocouple along the resonator's axis;  
 238 this simply means that the temperature field is not uniform through the cross  
 239 sectional area of the resonator. At time  $t \approx 75$ s, the onset of self-sustained  
 240 thermoacoustic oscillations clearly appears on the data depicted in Fig. 7.  
 241 However, as soon as the onset occurs these data are not reliable because  
 242 the sampling rate (1 Hz) is much lower than the acoustic frequency, and  
 243 also because equation (10) can no longer be used to calculate temperature  
 244 variations from density variations (the pressure being no longer constant).  
 245 As a result, only the temperature data on the left of the vertical dashed line  
 246 in Fig. 7 are worth considering, and finally the data obtained once the onset  
 247 of self-sustained oscillations has occurred will be the ones captured with the  
 248 high speed camera, while only density fluctuations (instead of temperature  
 249 fluctuations) will be presented in the following.

250 In Fig. 8, the time-resolved variations of both acoustic pressure (a,a')  
 251 and density (b-e) are presented. Acoustic pressure fluctuations are measured  
 252 by the microphone at position  $x = d$  during the whole transient regime,  
 253 while density fluctuations are measured during 4 seconds once the high speed  
 254 camera is triggered at time  $t \approx 77$ s. The time variations of density are  
 255 presented for four axial positions, namely  $x_1 = 1.3$  mm,  $x_2 = 3$  mm,  $x_3 = 4.7$   
 256 mm, and  $x_4 = 6.4$  mm. As clearly seen in Fig. 8, the starting point and the  
 257 duration of data acquisition coincides with the final stage of wave amplitude  
 258 growth, up to its saturation to a finite amplitude (after an overshoot process  
 259 which occurs around  $t \approx 78.3$  s). The same dynamical range (i.e. from 0.7  
 260 up to  $1.2 \text{ kg.m}^{-3}$ ) is used in the presentation of the densities  $\langle \rho \rangle (x_i, t)$   
 261 in Figs. 8(b-e). This enables to see clearly that the amplitude of density  
 262 oscillations strongly depend on the observation point  $x_i$ : these amplitudes  
 263 are much higher at positions  $x_1$  and  $x_2$  than at positions  $x_3$  and  $x_4$ . It is worth  
 264 pointing out that the distance  $x_4 - x_1$  (about 5 mm) is much lower than the  
 265 acoustical wavelength (about 2 m), which means that the observed variations  
 266 are not related to standard acoustic propagation. In other words, if the  
 267 measured density fluctuations were only related to the presence of a standing

268 acoustic wave, then the amplitude at position  $x_4$  should be the same as the  
 269 one at position  $x_1$ . Therefore, the fluctuations of density presented in Fig  
 270 8 (c-e) emphasize the presence of entrance effects. We use this terminology  
 271 (entrance) to refer to some effects associated to the abrupt transition at the  
 272 ends of the stack. These entrance effects have two natures: one is related  
 273 to the geometrical singularity at the end of the stack which leads to flow  
 274 separation (and possibly vortex shedding) and viscous dissipation, while the  
 275 other one is related to a singularity in terms of heat transfer due to the  
 276 fact that a gas parcel oscillating next to the end of the stack experiences  
 277 an abrupt transition between a polytropic motion (inside the stack) and an  
 278 essentially adiabatic motion (outside the stack).

279 Further analysis of the experimental data is provided in Fig. 9, where  
 280 the slow variations (as compared with the period of oscillations) of the mean  
 281 density are plotted as a function of time during the four seconds of mea-  
 282 surements. More precisely, the sliding average (denoted  $\rho_m$ ) over 17 acoustic  
 283 periods (with a 50 % time-recovery) computed from the raw data  $\langle \rho(x, t) \rangle$  is  
 284 presented as a function of time and for different positions  $x$ . The results of  
 285 Fig. 9 clearly exhibit a significant variation of the mean density, which also  
 286 strongly depends on the distance from the stack. There is indeed a signifi-  
 287 cant decrease of  $\rho_m$  occurring around  $t \approx 78.5$  s (i.e. around the overshoot of  
 288 acoustic pressure amplitude): this decrease can reach about 7 % of the initial  
 289 value (at time  $t = 77$  s) at a distance of about 1.8 or 2.4 mm from the stack,  
 290 while it is less than 2 % at  $x = 0.2$  mm and at  $x = 5.8$  mm. Such experimen-  
 291 tal results therefore indicate that entrance effects are responsible for a mean  
 292 (i.e. non-oscillating) nonlinear mass transport phenomenon localized in the  
 293 vicinity (but not in direct contact) of the stack termination.

294 It is also interesting to analyze the spectral components of density fluctua-  
 295 tions, notably because previous theoretical [13] and experimental [21] studies  
 296 have shown that the stack termination should be responsible for higher har-  
 297 monics generation in temperature fluctuations (even if pressure fluctuations  
 298 should be monochromatic). It is therefore expected that the latter impact on  
 299 temperature fluctuations should also modify the spectral content of density  
 300 fluctuations. In Fig. 10 we present the amplitudes of the fundamental and the  
 301 second harmonic components of density fluctuations (obtained from the Fast  
 302 Fourier Transform of raw data during the four seconds of data acquisition),  
 303 as a function of the distance  $x$  from the hot side of the stack. Addition-  
 304 ally, a rough estimate of the quasi-static (i.e. slowly varying) component of  
 305 density fluctuations is also presented in Fig 10: this quasi-static amplitude

306 is evaluated from the absolute difference between the initial mean density  
 307  $\rho_m(x, t = 77s)$  and its time-average  $\overline{\rho_m}$  during the four seconds of data ac-  
 308 quisition. It is also interesting to evaluate the expected peak amplitude that  
 309 density fluctuations should have if both the stack and the temperature gra-  
 310 dient were absent. Such a reference amplitude, denoted  $\rho_{ad}$ . in the following,  
 311 can be obtained from the microphone signal and from the assumption that  
 312 an adiabatic process of plane wave propagation occurs along the resonator.  
 313 This leads to the following formula

$$\rho_{ad} = \overline{P_{mic}} \cos(kd) / c_0^2 \quad (11)$$

314 where  $\overline{P_{mic}}$  stands for the peak amplitude of the microphone signal aver-  
 315 aged along the four seconds of data acquisition, and where  $k = 2\pi f / c_0$  is  
 316 the acoustical wave number. This reference amplitude of the fundamental  
 317 component is (almost) independent of position  $x$  since the width of optical  
 318 beam is here much lower than the acoustical wavelength. From the results  
 319 presented in Fig 10, there exist a significant distortion of density fluctuations  
 320 in the vicinity of the stack, since the amplitude of the second harmonic is  
 321 not small compared to that of the fundamental (especially around  $x \approx 4 - 5$   
 322 mm where the amplitude of the second harmonic can reach about 20 % of  
 323 the fundamental). It is also clear that the spatial distribution of both the  
 324 fundamental and the second harmonic components strongly depend on the  
 325 distance  $x$  from the stack. From the comparison of the measured amplitudes  
 326 and the one predicted from the microphone signal (dashed line), we can con-  
 327 clude once again that the results exhibit the impact of entrance effects, since  
 328 far from the stack, the measured amplitude of the fundamental component  
 329 tends towards the predicted amplitude  $\rho_{ad}$  while the amplitudes of both the  
 330 second harmonic and the quasi-static components tend towards zero.

#### 331 4. Discussion

332 The results of Fig. 10 confirm previous experimental[11, 18, 21], numerical[11,  
 333 21] or analytical[13] studies, whose main conclusions state that there exists  
 334 complicated heat and mass transport phenomena next to the ends of a stack.  
 335 However, a new point here is that we measured density fluctuations (instead  
 336 of velocity or temperature fluctuations), but also that the device we studied  
 337 is a self-sustained thermoacoustic oscillator (instead of a stack at room tem-  
 338 perature submitted to an acoustic wave by an external sound source), which

339 notably means that there exists also a steep temperature gradient at the  
 340 location where measurement are processed. Moreover, we did not proceed  
 341 to measurement during a controlled steady-state regime of acoustic oscilla-  
 342 tions, but instead during the transient regime of wave amplitude growth. As  
 343 a result, it is not straightforward to compare our experimental data with  
 344 any analytical/numerical model describing a situation identical to the one  
 345 we analyzed.

346 An attempt is made in the following to compare our experimental data  
 347 with the simplified analytical model provided by Gusev et al. [13]. This  
 348 model enables to evaluate the distortion of temperature fluctuations experi-  
 349 enced by gas parcels oscillating through the stack termination. Because  
 350 such a problem is generally not tractable analytically, some simplifications  
 351 are required and it is therefore assumed (1) that the fluid is inviscid, (2)  
 352 that the stack plates are infinitely thin and have an infinite thermal conduc-  
 353 tivity, (3) that the static temperature is constant at room temperature, (4)  
 354 that the axial conduction in the fluid is neglected while (5) transverse heat  
 355 conduction inside the stack is taken into account via a phenomenological pa-  
 356 rameter (equivalent to using a Newton's law of cooling with an arbitrarily  
 357 fixed heat transfer coefficient). Finally, assuming that the fluid is submitted  
 358 to a standing acoustic wave at angular frequency  $\omega = 2\pi f$  in the frame of  
 359 the linear acoustics approximation (and therefore without any distortion of  
 360 the pressure and velocity field next to the stack termination in the inviscid  
 361 fluid), and accordingly with the notation used in ref.[13], this results in the  
 362 following equation for a dimensionless gas temperature  $\theta$  [see ref. [13] for  
 363 more details]:

$$\frac{\partial \theta}{\partial \tau} + \sin \tau \frac{\partial \theta}{\partial \xi} = \sin \tau - \frac{\theta}{R}, \quad (12)$$

364 where  $\tau$  and  $\xi$  are dimensionless variables defined as  $\tau = \omega t$  and  $\xi = x/u$ ,  
 365 and where  $u$  stands for the peak amplitude of the gas displacement at the  
 366 location of the stack. In Eq. (12), the dimensionless temperature is defined  
 367 as  $\theta = T'/T_c$  where  $T_c$  is a characteristic amplitude of adiabatic temperature  
 368 fluctuations in a standing wave, while the parameter  $R$  is a dimensionless  
 369 relaxation time used to account for the thermal coupling between the gas  
 370 and the stack walls. In the following, we will consider that inside the stack  
 371 ( $\xi \leq 0$ ) one has  $R = 1$  while outside the stack ( $\xi \geq 0$ ) it tends towards  
 372 infinity: this assumption amounts to considering that the distance between  
 373 two stack plates is such that the thermoacoustic process is optimum ( $R = 1$ )

374 while the process is purely adiabatic outside the stack ( $R \rightarrow \infty$ ). Note that  
 375 both the characteristic amplitudes of gas displacement  $u$  and temperature  
 376 fluctuations  $T_c$  can be obtained from the (time-averaged) peak amplitude  
 377 of pressure fluctuations measured by the microphone as follows (accordingly  
 378 with ref. [13]):

$$u = \frac{\overline{kP_{mic.}}}{\rho_0\omega^2} \tan(kd), \quad (13)$$

$$T_c = -\frac{\overline{P_{mic.}}}{\rho_0 C_p} \cos(kd). \quad (14)$$

379 As shown by Gusev et al. [13], Eq. (12) can be solved analytically. In the  
 380 following, we provide the solution in the domain  $\xi \geq 0$ , which is written as:

$$\theta = -\frac{1}{2} \left[ \xi + \cos \tau + \sin(\tau_+) \left( 1 - \frac{e^{-\tau_+}}{\sinh(\tau_+)} \right) \right] \quad (15)$$

381 if  $|\xi + \cos \tau| \leq 1$ , with  $\tau_+ = \arccos(\xi + \cos \tau)$ , and

$$\theta = -\cos \tau \quad (16)$$

382 if  $|\xi + \cos \tau| \geq 1$ . This solution is valid outside the stack region  $\xi \geq 0$   
 383 to  $\xi = 2$  (i.e. up to the distance by which an oscillating gas parcel may  
 384 cross the stack during a cycle) and for  $\tau \in [-\pi, \pi]$ . From the Fourier se-  
 385 ries expansion of the solution  $\theta(\xi, \tau)$ , it is then straightforward to get the  
 386 amplitudes of the mean (time-averaged), the fundamental and the harmonic  
 387 components of  $\theta$  as a function of its mean position  $\xi$ . Finally, turning back to  
 388 dimensional amplitudes  $T'(x, t)$ , it is possible to plot the predicted spectral  
 389 components of temperature fluctuations as a function of the distance  $x$  from  
 390 the hot side of the stack. To that purpose we use  $d = 24$  cm,  $\overline{P_{mic.}} \approx 548$  Pa,  
 391 and  $f = 171.2$  Hz as input parameters, which corresponds to the experimen-  
 392 tal data, and which results in  $|T_c| \approx 1.17$  K and  $u = 1.2$  mm. The results  
 393 obtained for the fundamental, the harmonic and the time-averaged ( $\sim$  quasi-  
 394 static) components of temperature fluctuations are presented in Fig 11(a).  
 395 Such results reveal that, because of the singularity in term of heat transfer  
 396 at the stack termination, there exists a significant generation of the second  
 397 harmonic as well as a mean component of temperature, while the fundamen-  
 398 tal component itself varies significantly along the axis. It is predicted from  
 399 this model that these entrance effects extend up to twice the displacement

400 amplitude  $u$ , and that only the fundamental component remains for  $x \geq 2u$   
401 (with a peak amplitude  $T_c$ ). The spatial distribution of both the funda-  
402 mental and the second harmonic of temperature fluctuations presents some  
403 similarities with the experimental data of Fig. 10: one can notably remark  
404 that in both cases there exists a minimum for the amplitude of the second  
405 harmonic which is located at some position which roughly corresponds to the  
406 maximum of the fundamental. However, the data presented in Fig. 11(a)  
407 cannot be directly compared to those of Fig. 10, since the former deals with  
408 temperature while the latter deals with density. Therefore, the theoretical  
409 variations of the spectral components of density fluctuations as a function of  
410 position  $x$  are presented in Fig. 11(b). These variations are calculated from  
411 the temperature fluctuations using the linearized ideal gas law:

$$\rho'(x, t)/\rho_0 = p'(x, t)/P_0 - T'(x, t)/T_0 \quad (17)$$

412 in which the pressure fluctuations are perfectly harmonic (as initially assumed  
413 in the model) and almost independant of axial position  $x$  (since  $2u \ll c_0/f$ ):

$$p'(x, t) \approx \overline{P_{mic.}} \cos(kd) \cos(\omega t). \quad (18)$$

414 For a better readability we did not use the same dynamical range in Fig.  
415 11(b) as the one used in Fig. 10, but it is worth pointing out that the range  
416 of variation of  $\rho'$  is much higher in experiments (i.e. up to  $\approx 0.05 \text{ kg.m}^{-3}$ )  
417 than in the model (up to  $\approx 0.005 \text{ kg.m}^{-3}$ ). There is therefore a significant  
418 discrepancy between the simplified model and the experimental results, and  
419 the model underestimates the maximum amplitudes of the fundamental (fac-  
420 tor  $\times 10$ ), the second harmonic (factor  $\times 5$ ) and the quasi-static (factor  $\times 8$ )  
421 components. Also, while the model predicts that entrance effects extend up  
422 to  $\approx 2.5 \text{ mm}$ , the experiments show that the entrance effects extend up to  
423  $\approx 6 \text{ mm}$ . Such an extension of the impact of entrance effects beyond the  
424 distance  $2u$  has already been reported by Berson et al.[21] both numerically  
425 and experimentally (from the measusurement of  $T'$  using cold wire anemom-  
426 etry), and can be explained (at least partially) by accounting for the axial  
427 conduction within the fluid in Eq. (12). However, the large discrepancy in  
428 terms of amplitudes as well as the differences in terms of spatial distribu-  
429 tion (notably for the fundamental and the quasi-static components) is not  
430 explained. The model used here is based on numerous assumptions, but it  
431 has the merits to emphasize that the observed experimental results cannot  
432 be only explained by an abrupt transition in terms of heat transfer at the



433 stack interface. We believe that the more drastic assumption made here is  
434 that of an inviscid fluid, which means that aerodynamical effects like flow  
435 separation, vortex shedding, or possibly jet-driven streaming are not con-  
436 sidered, and the resulting nonlinear heat and mass transport by the above  
437 mentioned effects is not considered. Both aerodynamical entrance effects and  
438 the presence of a steep temperature gradient should therefore be considered  
439 in the modeling to get a better agreement. Such a task falls out of the scope  
440 of this paper, and the important point is that the experiments reveal that  
441 the impact of entrance effects on density is very significant. As a result, the  
442 possible impact of such entrance effects on the dynamics of wave amplitude  
443 growth in thermoacoustic devices is worth considering for future works.

## 444 5. Conclusion

445 This paper presents an interferometric holographic measurement tech-  
446 nique which has been successfully applied to the measurement of density  
447 fluctuations associated to acoustic oscillations in a thermoacoustic prime-  
448 mover. To our knowledge, such a technique has not been applied to acoustics  
449 or thermoacoustics, except for the analogous holography technique used by  
450 Wetzel and Herman in the late 90's [25, 26, 27]. This measurement technique  
451 appears to be a simple and promising way to get further insight into the oper-  
452 ation of thermoacoustic engines (and, maybe, into other acoustical problems)  
453 as a complementary tool to other techniques like Particle Image Velocimetry  
454 or Cold Wire Anemometry. Although the results presented in this paper  
455 remain unexplained because of the lack of an appropriate model, they re-  
456 veal that the stack termination generates both gas rarefaction and higher  
457 harmonics generation in the vicinity of the stack termination. The magni-  
458 tude of the effect is such that, beyond the only dissipation of acoustical work  
459 it causes (minor losses), the question of its impact on the thermoacoustic  
460 process (wave amplification and thermoacoustic heat flux within the stack)  
461 should be considered cautiously for future works.

## 462 Acknowledgments

463 This research was funded from the French National Agency for Research  
464 under grant agreement ANR 2010 BLAN 0302 01.



465 **Bibliography**

- 466 [1] G.W. Swift, *Thermoacoustics: A unifying perspective for some engines*  
467 *and refrigerators*, Acoustical Society of America, Melville NY (2001).
- 468 [2] N. Rott, *Thermoacoustics*, *Adv. Appl. Mech.* 20 (1980) 135-175.
- 469 [3] J. Wheatley, T.J. Hofer, G. W. Swift, A. Migliori, *Understanding some*  
470 *simple phenomena in thermoacoustics with applications to acoustical*  
471 *heat engines*, *Am. J. phys.*, 53 (1985) 147-162.
- 472 [4] G.W. Swift, *Analysis and performance of a large thermoacoustic engine*,  
473 *J. Acoust. Soc. Am.* 92 (1992) 1551-1563.
- 474 [5] S.L. Garrett, J.A. Adef, T.J. Hofer, *Thermoacoustic refrigerator for*  
475 *space applications*, *J. of Thermophysics and Heat Transfer*, 7 (1993)  
476 595-599.
- 477 [6] S. Backhaus, G.W. Swift, *A thermoacoustic Stirling heat engine*, *Nature*  
478 399 (1999) 335-338.
- 479 [7] S. Backhaus, E. Tward, M. Petach, *Traveling-wave thermoacoustic elec-*  
480 *tric generator*, *Appl. Phys. Lett.* 85 (2004) 1085-1087.
- 481 [8] M.E.H. Tijani, S. Spoelstra, *A high performance thermoacoustic engine*,  
482 *J. Appl. Phys.* 110 (2011) 093519.
- 483 [9] Z. Wu, G. Yu, L. Zhang, W. Dai, E. Luo, *Development of a 3 kW double-*  
484 *acting thermoacoustic Stirling electric generator*, *Applied Energy* 136  
485 (2014) 866-872.
- 486 [10] S. Boluriaan, P.J. Morris, *Acoustic streaming: from Rayleigh to today*,  
487 *Int. J. of Aeroacoustics* 2 (2003) 255-292.
- 488 [11] Ph. Blanc-Benon, E. Besnoin, O. Knio, *Experimental and computational*  
489 *visualization of the flow field in a thermoacoustic stack*, *C. R. Mec.* 331  
490 (2003) 1724.
- 491 [12] C. Scalo, S.K. Lele, L. Hesselink, *Linear and nonlinear modelling of a*  
492 *theoretical travelling-wave thermoacoustic heat engine*, *J. Fluid Mech.*,  
493 766 (2015) 368-404.

- 494 [13] V. Gusev, P. Lotton, H. Bailliet, S. Job, M. Bruneau, Thermal wave  
495 harmonics generation in the hydrodynamical heat transport in thermoacoustics,  
496 *J. Acoust. Soc. Am.* 109 (2001) 84-90.
- 497 [14] M.W. Thompson, A.A. Atchley, Simultaneous measurement of acoustic  
498 and streaming velocities in a standing wave using laser Doppler anemometry,  
499 *J. Acoust. Soc. Am.* 117 (2005) 1828-1838.
- 500 [15] S. Moreau, H. Bailliet, J.C. Valire, Measurements of inner and outer  
501 streaming vortices in a standing waveguide using laser Doppler velocimetry,  
502 *J. Acoust. Soc. Am.* 123 (2008) 640-647.
- 503 [16] C. Desjoux, G. Penelet, P. Lotton, J. Blondeau, Measurement of acoustic  
504 streaming in a closed-loop traveling wave resonator using Laser Doppler  
505 Velocimetry, *J. Acoust. Soc. Am.* 126 (2009) 2176-2183.
- 506 [17] I. Reyt, H. Bailliet, J.C. Valire, Experimental investigation of acoustic  
507 streaming in a cylindrical wave guide up to high streaming Reynolds  
508 numbers, *J. Acoust. Soc. Am.* 135 (2014) 27-37.
- 509 [18] A. Berson, Ph. Blanc-Benon, Nonperiodicity of the flow within the gap  
510 of a thermoacoustic couple at high amplitudes, *J. Acoust. Soc. Am.* 122  
511 (2007) EL122-EL127.
- 512 [19] A.J. Jaworski, X. Mao, X. Mao, Z. Yu, Entrance effects in the channels  
513 of the parallel plate stack in oscillatory flow conditions, *Exp. Therm.  
514 Fluid Sci.* 33 (2009) 495-502.
- 515 [20] L. Shi, Z. Yu, A.J. Jaworski, Vortex shedding flow patterns and their  
516 transitions in oscillatory flows past parallel-plate thermoacoustic stacks,  
517 *Exp. Therm. Fluid Sci.* 34 (2010) 954-965.
- 518 [21] A. Berson, G. Poignand, Ph. Blanc-Benon, G. Comte-Bellot, Nonlinear  
519 temperature field near the stack ends of a standing-wave thermoacoustic  
520 refrigerator, *Int. Journ. Heat Mass Transfer* 54 (2011) 4730-4735.
- 521 [22] P. Picart, J. Leval, F. Piquet, J.P. Boileau, J.P. Dalmont, Analysis of  
522 Clarinet Reed Oscillations With Digital Fresnel Holography, *Europ. J.  
523 Phys. Appl. Phys.* 47 (2009) 12706.

- 524 [23] M. Leclercq, M. Karray, V. Isnard, F. Gautier, P. Picart, Evaluation  
525 of surface acoustic waves on the human skin using quasi-time-averaged  
526 digital Fresnel holograms, *Appl. Optics*. 52 (2013) A136-A146.
- 527 [24] J.M. Desse, P. Picart, P. Tankam, Digital color holography applied to  
528 fluid and structural mechanics, *Optics and Laser in engin.*, 50 (2012)  
529 18-28.
- 530 [25] M. Wetzel, C. Herman, Limitations of temperature measurements with  
531 holographic interferometry in the presence of pressure variations, *Exp.*  
532 *Therm. Fluid Sci.* 17 (1998) 294-308.
- 533 [26] M. Wetzel, C. Herman, Experimental study of thermoacoustic effects on  
534 a single plate Part I: Temperature fields, *Heat Mass Transf.* 36 (2000)  
535 7-20.
- 536 [27] M. Wetzel, C. Herman, Experimental study of thermoacoustic effects  
537 on a single plate Part II: Heat transfer, *Heat Mass Transf.* 35 (1999)  
538 433-441.
- 539 [28] T. Leitgeb, T. Schuller, D. Durox, F. Giuliani, S. Koberl, J. Woit-  
540 setschlager, Interferometric determination of heat release rate in a pul-  
541 sated flame, *Combustion and flame* 160 (2013) 589-600.
- 542 [29] Y. Miura, S. Yoshihara, M. Ohnishi, K. Honda, M. Matsumoto, J.  
543 Kawai, M. Ishikawa, H. Kobayashi, A. Onuki, High-speed observation  
544 of the piston effect near the gas-liquid critical point, *Phys. Rev. E* 74  
545 (2006) 010101.
- 546 [30] G. Penelet, T. Biwa, synchronization of a thermoacoustic oscillator by  
547 an external sound source, *American Journ. Phys.*, 81 (2013) 290-297.
- 548 [31] G. Penelet, M. Guedra, V. Gusev, T. Devaux, Simplified account of  
549 Rayleigh streaming for the description of nonlinear processes leading to  
550 steady state sound in thermoacoustic engines, *Intern. Journ. Heat Mass*  
551 *Transfer*, 55 (2012) 6042-6053.
- 552 [32] M. Guedra, G. Penelet, P. Lotton, Experimental and theoretical study  
553 of the dynamics of self-sustained oscillations in a standing wave ther-  
554 moacoustic engine , *J. Appl. Phys.* 115 (2014) 024504.

- 555 [33] I. Yamaguchi, T. Zhang, Phase shifting digital holography, Optics Let-  
556 ters 22 (1997) 1268-1270.
- 557 [34] E. Cuche, F. Bevilacqua, C. Depeursinge, Digital holography for quan-  
558 titative phase contrast imaging, Optics Letters 24 (1999) 291-293.
- 559 [35] U. Schnars and W. Jptner, Direct recording of holograms by a CCD  
560 target and numerical reconstruction, Appl. Opt. 33 (1994) 179-181.
- 561 [36] J. Desse, P. Picart, and P. Tankam, Digital three-color holographic in-  
562 terferometry for flow analysis, Opt. Express 16 (2008) 5471-5480.
- 563 [37] J. Li, P. Tankam, Z. Peng, and P. Picart, Digital holographic recon-  
564 struction of large objects using a convolution approach and adjustable  
565 magnification, Opt. Lett. 34 (2009) 572-574.
- 566 [38] P. Picart, P. Tankam, D. Mounier, Z. Peng, and J. Li, Spatial band-  
567 width extended reconstruction for digital color Fresnel holograms, Opt.  
568 Express 17 (2009) 9145-9156.
- 569 [39] D.C. Ghiglia, M.D. Pritt, Two-Dimensional Phase Unwrapping : The-  
570 ory, Algorithms and Software, Wiley Ed., New York (1998).

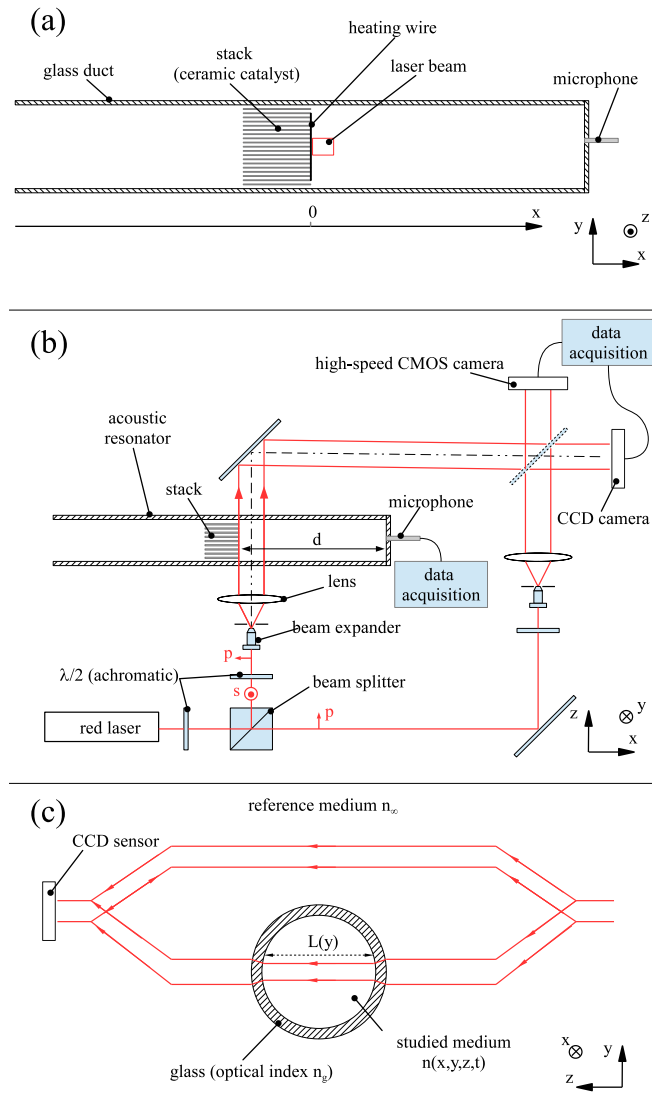


Figure 1: Sketch of the experimental apparatus, including the thermoacoustic oscillator (a) and the optical set-up (b) which basically consists of a reference beam and a measurement beam passing through the acoustic resonator (c) close to the heated end of the stack.

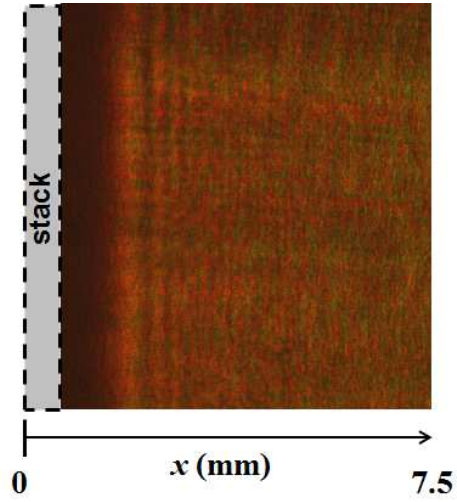


Figure 2: An example of a digitally recorded hologram. The stack is located on the left hand side of the picture.

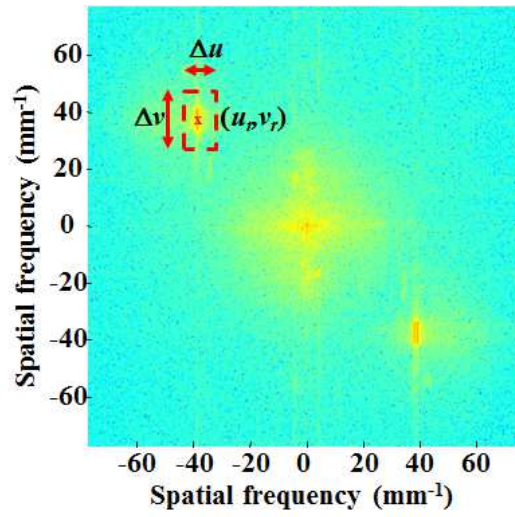


Figure 3: Spatial Fourier spectrum of the recorded hologram.

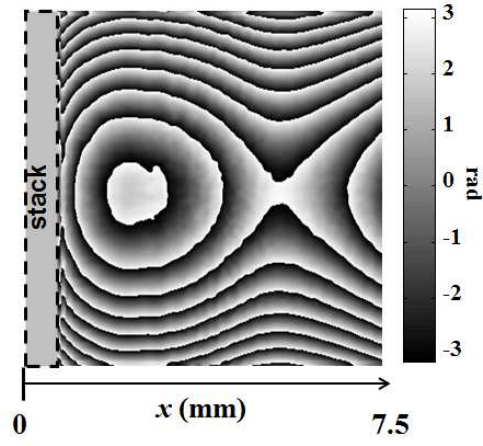


Figure 4: Phase map extracted from the filtered Fourier spectrum of Fig. 3

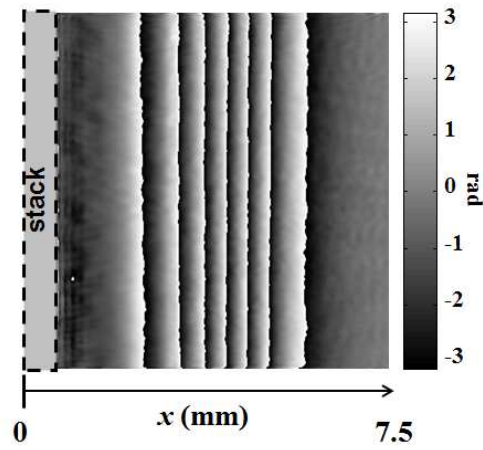


Figure 5: Phase difference  $\Delta\varphi_\lambda$  between the current state and a reference state (e.g. neither heating nor acoustic wave) as a function of  $x$  and  $y$ .

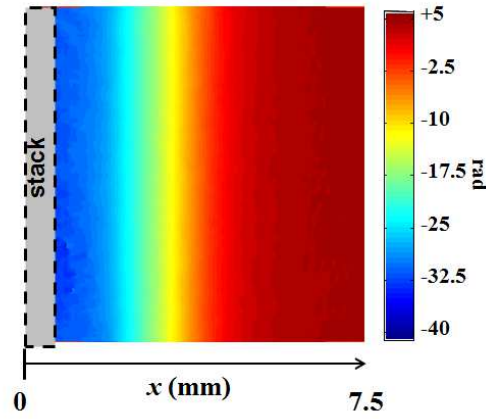


Figure 6: Phase difference  $\Delta\varphi_\lambda$  between the current state and a reference state (e.g. neither heating nor acoustic wave) as a function of  $x$  and  $y$  after the process of phase unwrapping.

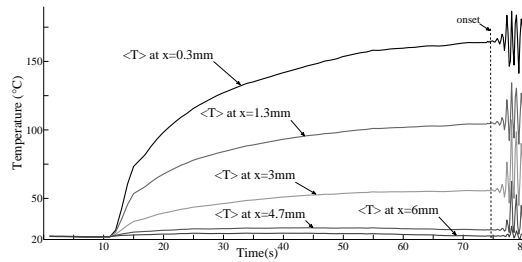


Figure 7: Variations as a function of time of the temperature next to the heated side of the stack during the process of heat supply, for different positions along the resonator's axis. These temperatures, obtained from digital holograms and the ideal gas law, are averaged temperature along the line of sight of the probe beam through the resonator. The reference position  $x = 0$  corresponds to the heated side of the stack.



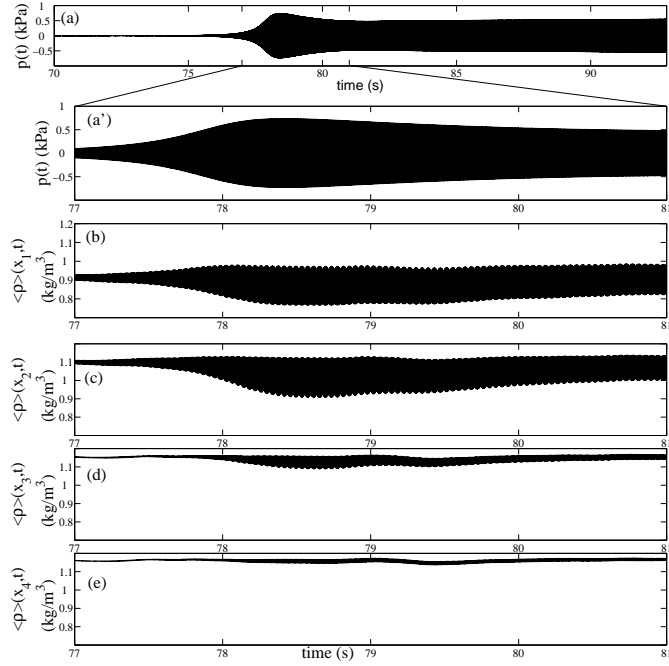


Figure 8: Acoustic pressure (a,a') and density (b-e) fluctuations as a function of time during the transient regime of wave amplitude growth. The measurement of density fluctuations  $\rho(x_i, t)$  are processed during 4 seconds from the holograms sensed by the high speed camera at a sampling rate of 1kHz. Axial positions  $x_i$  correspond to  $x_1 = 1.3$  mm,  $x_2 = 3$  mm,  $x_3 = 4.7$  mm, and  $x_4 = 6.4$  mm.

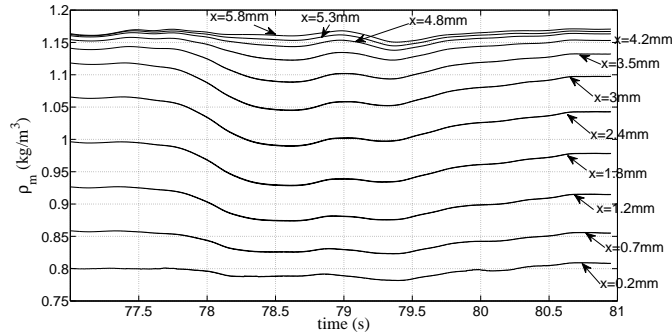


Figure 9: Quasi-static, acoustically induced variations of the mean density  $\rho_m$  as a function of time and axial position  $x$  ( $x=0$  refers to the hot side of the stack). These quasi-static variations are evaluated from  $\langle \rho' \rangle(x, t)$  using a sliding average over 100 successive sample images (i.e. during  $\approx 17$  acoustic periods) with a 50 % recovery.

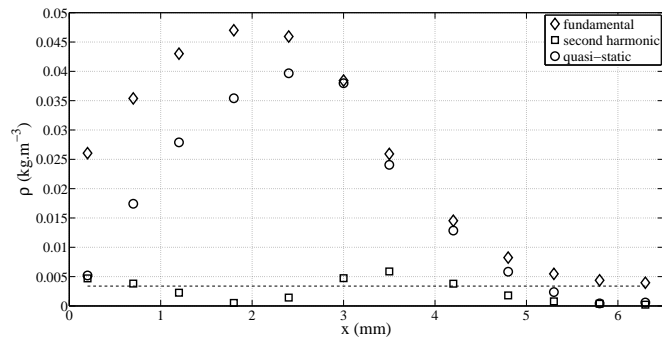


Figure 10: Amplitudes of the fundamental ( $\diamond$ ), the second harmonic ( $\square$ ) and the quasi-static ( $\circ$ ) components of density fluctuations obtained in experiments as a function of axial position  $x$ . In addition, the horizontal dashed line corresponds to the peak amplitude of density fluctuations estimated from the microphone signal using the assumption of a linear and adiabatic process of acoustic propagation. Note that the evaluated peak amplitude of gas displacement for this configuration is  $u \approx 1.2$  mm.

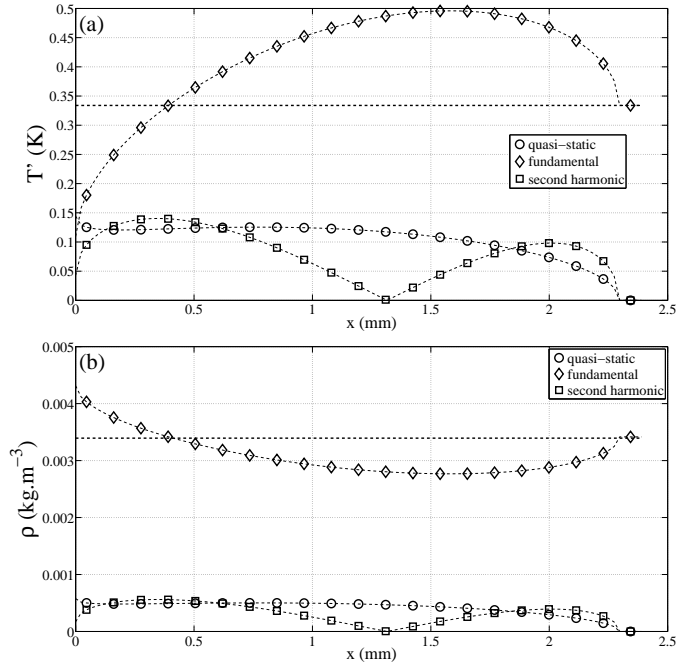


Figure 11: Theoretical amplitudes of the fundamental ( $\diamond$ ), the second harmonic ( $\square$ ) and the quasi-static ( $\circ$ ) components of both temperature (a) and density (b) fluctuations as a function of axial position  $x$ . In addition, the horizontal dashed lines correspond to the peak amplitude of temperature (a) and density (b) fluctuations estimated from the microphone signal using the assumption of a linear and adiabatic process of acoustic propagation. Note that the evaluated peak amplitude of gas displacement for this configuration is  $u \approx 1.2$  mm.